

Vortex dynamics in a plane, moderate-Reynolds-number shear layer

By E. PANIDES¹ AND R. CHEVRAY²

¹Mechanical Engineering Sciences Laboratory, North Tarrytown, NY 10591, USA

²Department of Mechanical Engineering, Columbia University, New York, NY 10027, USA

(Received 4 October 1988 and in revised form 19 October 1989)

A completely non-intrusive technique, utilizing synchronized flow visualization and one-point, two-component laser-Doppler velocimetry, has been developed to examine the vortical structure of a homogeneous plane shear layer at a moderate Reynolds number. Results include ensemble-averaged velocity and vorticity maps and, derived from these data, zone-averaged statistics of the basic structure, at 6.2 initial wavelengths downstream of the splitter-plate trailing edge. The velocity field data paint a clear picture of the processes involved in the engulfment or entrainment of free-stream irrotational fluid by the vortices, and the evolution of the material interface separating fluid from the two free streams. The ensemble-averaged vorticity distribution is seen to be of an elliptical cross-section, closely resembling that of the Stuart vortex for a vorticity distribution parameter of 0.4. The effect of jitter which, in the case of zone averages is effectively removed, is assessed by comparison to conventional mean flow properties. It is found that vortex jitter greatly influences u' and R_{uu} and, in confirmation of previous results, that a passive vortex does not contribute to the production of large-scale Reynolds stress.

1. Introduction

It is now well established that coherent structures, also referred to as vortical structures or simply vortices, are an intrinsic feature of turbulent shear flows, rather than insignificant remnants of the initial instability. They are known to play a vital role in the overall development of the flow and are largely responsible for entrainment and mixing. The plane shear layer, in particular, is endowed with structures possessing a high degree of coherence, primarily as the result of simple flow geometry along with the constant velocity difference that is maintained throughout the flow field. It is for this reason that in no other flow has such a clear picture (of coherent structures) emerged, as for the plane shear layer which, since the pioneering work of Brown & Roshko (1974) and Winant & Browand (1974), has been the focus of attention of numerous research efforts.

Even in the early stages of coherent structure research, the need for specialized conditional sampling techniques was recognized (Davies & Yule 1975), as conventional statistical descriptions are of little value in examining the quasi-periodic structures. As a result, a number of such techniques have been developed which can broadly be classified into two categories. One such technique consists in detecting the passage of a naturally occurring structure by monitoring some physical characteristic. With the selection of appropriate criteria, a particular point in time and/or space can be identified and, relative to it, ensemble averages can be formed at other points of the domain. A common arrangement has been to monitor the

streamwise fluctuations (induced by the passing vortices) with one sensor, while measuring with another (Browand & Weidman 1976; Yule 1978); peaks in the detector sensor's output are associated with the centre of the passing vortex. To account for the broad dispersion of structure characteristics (e.g. size, shape, orientation, etc.) several versions of this arrangement have evolved; in these, measurements are made by multi-sensor or an array of single sensor probes requiring elaborate data processing and pattern recognition algorithms (Mumford 1982; Hussain 1983). This category of conditional sampling techniques, however, is subject to the questions of subjectivity in the choice of detection criteria, or (when an effort is made to correct this) instrumentation and processing complexity. The alternative approach, comprising the second category of conditional sampling methods, has been to suppress the irregularity in the vortex structure of a natural shear layer. This is usually done by introducing small periodic perturbations into the flow; if the frequency of the external disturbance is near the natural frequency of the shear layer, the flow 'locks in' to this frequency, and the appearance of irregularity in its structure is delayed for considerable downstream distances (Ho & Huang 1982). Successive structures in the near field of a forced shear layer are therefore (very nearly) periodic and identical, so that, using the forcing frequency as a reference, ensemble averages can easily be measured (Zaman & Hussain 1980; Sokolov, Kleis & Hussain 1981). In alleviating the need for elaborate instrumentation hardware (and software) this is clearly a more attractive approach; still, one may question the relevance of the induced structures to the naturally occurring ones since, at least, a first generation vortex structure is bound to evolve differently in the well-organized environment of a forced shear layer, than it would in the random environment of a natural shear layer (Hussain 1983).

In general, most of the aforementioned conditional sampling methods require that two or more probes (typically hot wires or hot films) be inserted in the flow under investigation. An important consideration is the intrusiveness of these probes, since evidence (Dimotakis & Brown 1976; Hussain & Zaman 1978; Ho & Huang 1982) suggests the existence of a feedback mechanism, implying that probe interference would modify (if not disturb) the shear layer. Moreover, it has been pointed out (Chevray & Tutu 1978; Dimotakis, Debussy & Koochesfahani 1981) that in half-jets, instantaneous flow reversals are common. As such, in studying half-jets via conditional sampling, it is imperative that velocity measuring techniques capable of resolving flow direction, are incorporated.

Given this background, the objective of this investigation is to take a new approach, in an attempt to remedy some of the aforementioned problems in conditional sampling. This is done by utilizing flow visualization as the conditioning agent to synchronized (in time, to within 0.5 ms), one-point, two-component laser-Doppler velocimetry (LDV) velocity measurement; the detection scheme is therefore direct and objective. Furthermore, through flow visualization, in addition to being unambiguously detected, a vortex structure is completely characterized in terms of its size, orientation, position, etc.; information that is not available or can only be inferred with most conditional sampling methods. On the other hand, LDV is a common non-intrusive velocity diagnostic which, through electronic frequency shifting, is direction-sensitive. Thus, with the technique presented here, it is possible to examine the vortical structures in their natural (random) environment (rather than forcing the shear layer), in a straightforward and completely non-intrusive manner.

2. Experimental facilities and instrumentation

2.1. Flow apparatus

The experiments described herein were carried out in a wind tunnel 5.84 m in length, 1.02 m high and 15 cm wide, made entirely of aluminium. A splitter plate separated the wind tunnel into two sections whereby two independent airstreams were generated. In the contraction, the splitter plate was tapered to a fine trailing edge where the two parallel streams met. The diffuser and contraction sections had area ratios of 1:10 and 1:4 respectively. The settling chamber contained a set of honeycombs and a series of fine screens; as a result, the flow entering the test section was uniform to within 0.5% with free-stream turbulence intensity of 0.6% and 1.0% in the upper and lower streams respectively, for corresponding (typical) free-stream velocities of 2.0 m/s and 1.0 m/s.

The Plexiglas test section (1 m long, 25 cm high and 15 cm wide) was connected to the exhaust line of the building, in which a continuously on-line fan (far downstream of the wind tunnel) operated, thereby generating the airflow in the wind tunnel. Adjustment of the velocities in the two streams was accomplished by varying the flow resistance at the inlet section, via small screens of various mesh sizes. Since, in this mode of operation, the pressure in the wind tunnel was less than ambient, except for a large chamber (through which, filtered air is admitted) at the inlet, the wind tunnel was completely sealed. The advantage of this arrangement, it was determined, is that free-stream fluctuations are of very low frequency, well outside the receptivity zone of the shear layer. If, on the other hand, the air was forced through the wind tunnel (e.g. with a blower), higher and discrete frequencies would be introduced which may have adversely affected the shear layer.

Below the test section a steel channel section beam, oriented perpendicularly to the flow direction, was affixed to the bed of a milling machine. The flat surface of the beam provided a platform on which instruments were mounted (e.g. LDV, camera, etc.); using the milling machine these could be traversed in all three directions with an accuracy of 0.0254 mm. Flow conditions in the wind tunnel were assessed using hot-wire probes, placed just upstream of the splitter-plate trailing edge. Both boundary layers, above and below the splitter plate were laminar, in very good agreement with the Blasius profile, with shape factors of 2.59 and 2.46 respectively. Further details on initial conditions are given by Panides (1987).

2.2. Velocity measurements

All velocity measurements, with the exception of those described in the previous section, were made with a DISA laser-Doppler velocimeter. It is a helium-neon based, one colour, three beam system, capable of measuring two components of velocity using light polarization for discrimination. The flow was seeded with silicone oil particles, generated by a TSI 9306 atomizer. The resulting aerosol, of adjustable number density, was polydispersed with a mean particle diameter of about one micron. It is particularly well suited for this LDV system since, the particles being spherical in shape, the scattered light has the same polarization as the incident light.

To circumvent the problems of biasing and randomly spaced data, inherent in LDV measurements, the following procedure was used. The flow was seeded so as to observe (from the counter displays) 1.5 to 2.0 kHz data rates in both free streams, and no decrease in the validation rates (resulting from multi-particle scattering). The analog signals from the counters were low pass filtered (Krohn-Hite, 3202R) at a cutoff frequency of 1 kHz so that, the resulting filtered signals were smooth and

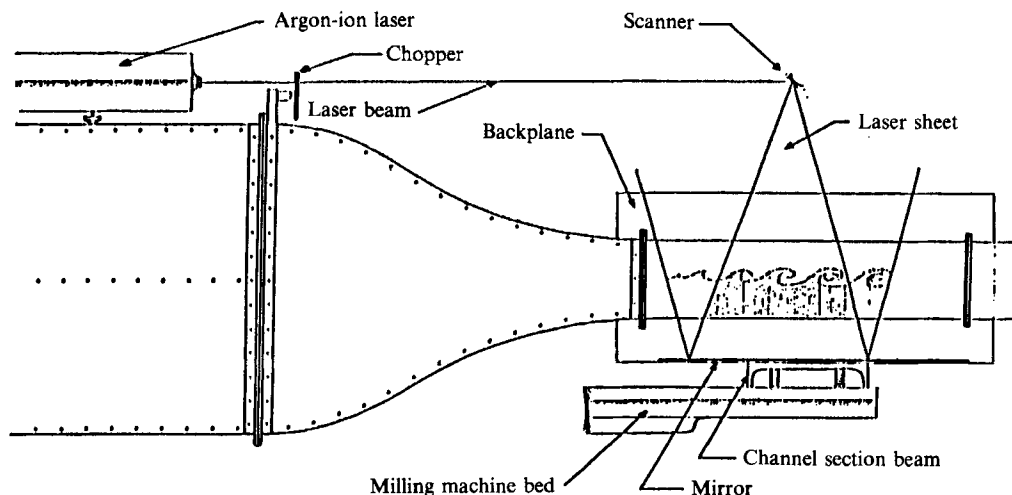


FIGURE 1. Side view of the set-up for flow visualization.

continuous much like a hot-wire signal; these were uniformly sampled at a rate of 2 kHz, as required by the sampling theorem.

2.3. Flow visualization

Since the two streams were seeded so as to observe approximately equal data rates in the free streams (see previous section), on the average, the (silicone oil) particle concentrations in the free streams were inversely proportional to the corresponding free-stream velocities (typically, $U_2/U_1 = 0.5$). Consequently, the interface was characterized by a sharp gradient in particle concentration, this being the basis for flow visualization.

Illumination was provided by a Spectra Physics 164-07, 5 W argon-ion laser. The laser was (carefully) mounted and secured on top of the wind tunnel, as shown in figure 1. A broadband rear reflector was inserted to allow output of light of several wavelengths, with 488 nm (blue) and 514.5 nm (green) being the two principal lines. The cyan beam was directed towards a General Scanning S23012 scanner (i.e. oscillating mirror), driven by a AX730 controller amplifier. The scanner oscillated at a fixed frequency of 1.2 kHz with an adjustable amplitude (maximum 30°, peak to peak); it was mounted on an 'L' beam directly above the test section and oriented so that the resulting laser sheet, and the plane formed by the streamwise and transverse directions, were one and the same. To further increase the amount of light, a flat mirror was placed on the platform directly underneath the test section. For improved contrast, a wooden backplane, painted flat black was positioned behind the test section. Finally, a chopper wheel, driven by a small d.c. motor, was placed in the path of the laser beam for strobing.

The silicone oil particles clearly had a dual role: to scatter the red, helium-neon laser light for the LDV to work and to scatter the cyan, argon-ion laser light for the flow to be visualized. For the reasons described earlier in this section, the slow stream fluid bearing a higher particle concentration appeared bright blue whereas the fast stream fluid appeared pale blue thus rendering the interface of the two readily visible. While the view was two-dimensional (the laser sheet was but a few millimetres thick), symptoms of three-dimensional motion could be discerned in the form of flow into, or out of, the laser sheet and 'blurring'.

There are several advantages of this flow visualization technique in comparison to other methods where only the interface is labelled (e.g. with smoke or dye). First, no additional provisions (for injecting the marker fluid), which may possibly disturb the flow, are necessary; thus, it is convenient and completely non-intrusive. Secondly, since the basis of the technique is the sharp concentration gradient at the interface, it offers superior clarity over conventional methods; the usual problems, arising from the rapid diffusion of the marker fluid are therefore alleviated. Furthermore, and perhaps more importantly, the flow visualization obtained with this technique is simpler to interpret. It should, however, be noted that aerosols are known to exhibit very large (typically 10^6) Schmidt numbers. While this property is advantageous for flow visualization purposes, it should be kept in mind that, as a result, the boundary of the aerosol bearing fluid does not precisely identify the actual (gas) interface. Nonetheless, it is estimated that this error is very small, given the moderate Reynolds number of the flow.

For documentation, 16 mm cinematography was chosen, using a Photo-Sonics 161PL movie camera with variable frame speed (24–500 frames/s $\pm 1\%$) and exposure time (1/54–1/24000 s), powered by a 28 VDC power supply. It was equipped with a 400 ft magazine allowing up to 400 ft film reels and a normal 25 mm $f/0.95$ Angenieux lens. The most important feature of the camera was a magnetic sensor, monitoring the rotation of a magnetized wheel that was directly coupled to the motor shaft and hence the shutter. The result was a pulse-like signal that could trace the motion of the shutter which, when synchronized, provided the link between flow visualization and simultaneous LDV measurements. Details of the synchronization technique are given in §3.1.

3. Procedures for simultaneous flow visualization and LDV measurements

3.1. Data acquisition

The movie camera and the LDV (transmitting and receiving optics) were mounted on the platform below the test section, as shown in figure 2. The lens was set at its widest aperture ($f/0.95$); the camera was loaded with Kodak 7250 colour film (400 ASA rating); a speed of 100 frames per second and an exposure time of 1/600 s were selected. The platform was traversed in the spanwise direction so as to position the LDV probe volume in the plane of the laser sheet. Adjustments were then made so that the camera lens and the LDV transmitting optics shared a common optical axis. The distance between the film plane and the laser sheet was 56 cm, permitting a flow region 15 cm in (streamwise) extent to be recorded on film. The three converging LDV beams (passing through the backplane via three small holes) appeared as a red cross, situated at the middle of the frame; when properly focused, the centre of the cross was a point, indicating the location of velocity measurement.

Synchronization was achieved in the following manner: with the camera running (at a constant speed), a DPST switch was turned on, simultaneously connecting a voltage source to two green LED's mounted on the backplane (visible to the camera) and a 2 kHz clock to the A/D converter of the data acquisition system. In all subsequent frames of the film, the LED's were lit and, in the meantime, the A/D collected the three channels of data (two signals from the LDV counters and one from the camera). In this way, the first frame with the LED's lit corresponded to the first pulse appearing in the resulting datafile, the second 'marked' frame to the second pulse, and so on. It was straightforward then to relate each such frame from the flow visualization to the corresponding measurements. With the data acquired at a rate

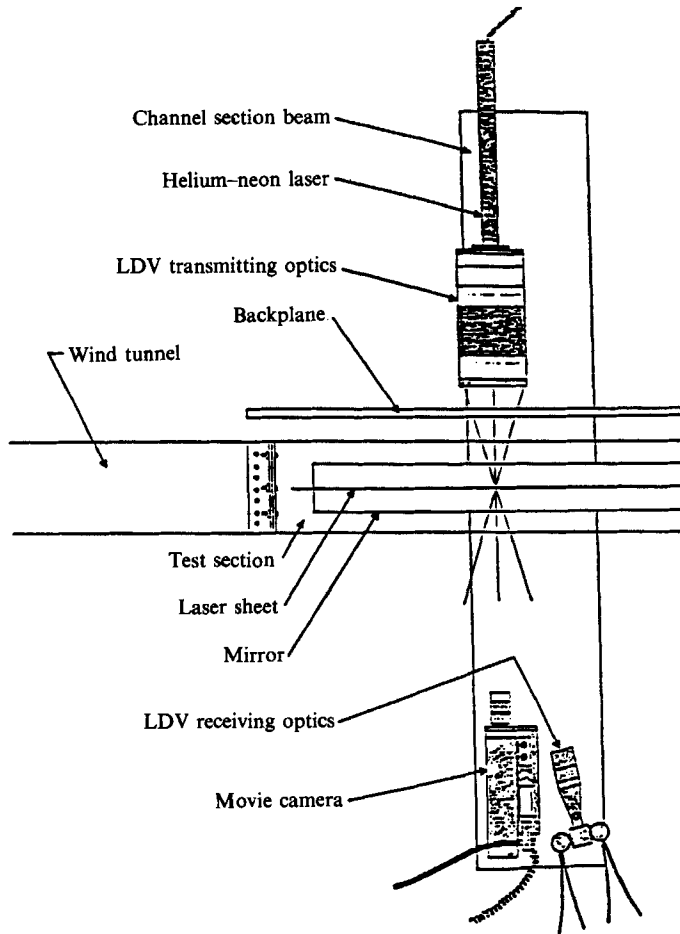


FIGURE 2. Top view of the set-up for simultaneous flow visualization and LDV velocity measurements.

of 2 kHz, synchronization was to within 0.5 ms since the exposure time was known ($1/600 \approx 1.5$ ms) and the pulse was obtained at the leading edge of the shutter opening.

3.2. Data analysis

Free-stream velocities of $U_1 = 1.8$ m/s (upper stream) and $U_2 = 0.9$ m/s (lower stream) were used throughout the course of these experiments. A broad view of the resulting shear layer is shown in the flow visualization sequence of figure 3, obtained by seeding only the lower slow stream so as to get the best possible contrast. The region of interest is indicated in frame 4; within it, it is noticed that only first generation vortices (i.e. those whose origin are instability waves of the splitter plate trailing edge) appear. As would be expected (of a natural shear layer) a broad range of vortex characteristics such as size, spacing and orientation, is observed. Thus, for example, the first vortex (pointed to by the arrow) in frame 2 is seen to convect passively downstream whereas, its preceding neighbour (the first vortex on the left of frame 3) has a much shorter lifetime, since it quickly coalesces with its preceding neighbour. Usually the vortices formed aperiodically but, on the average, a frequency of 45 Hz was measured by observing 500 successive frames. This value is

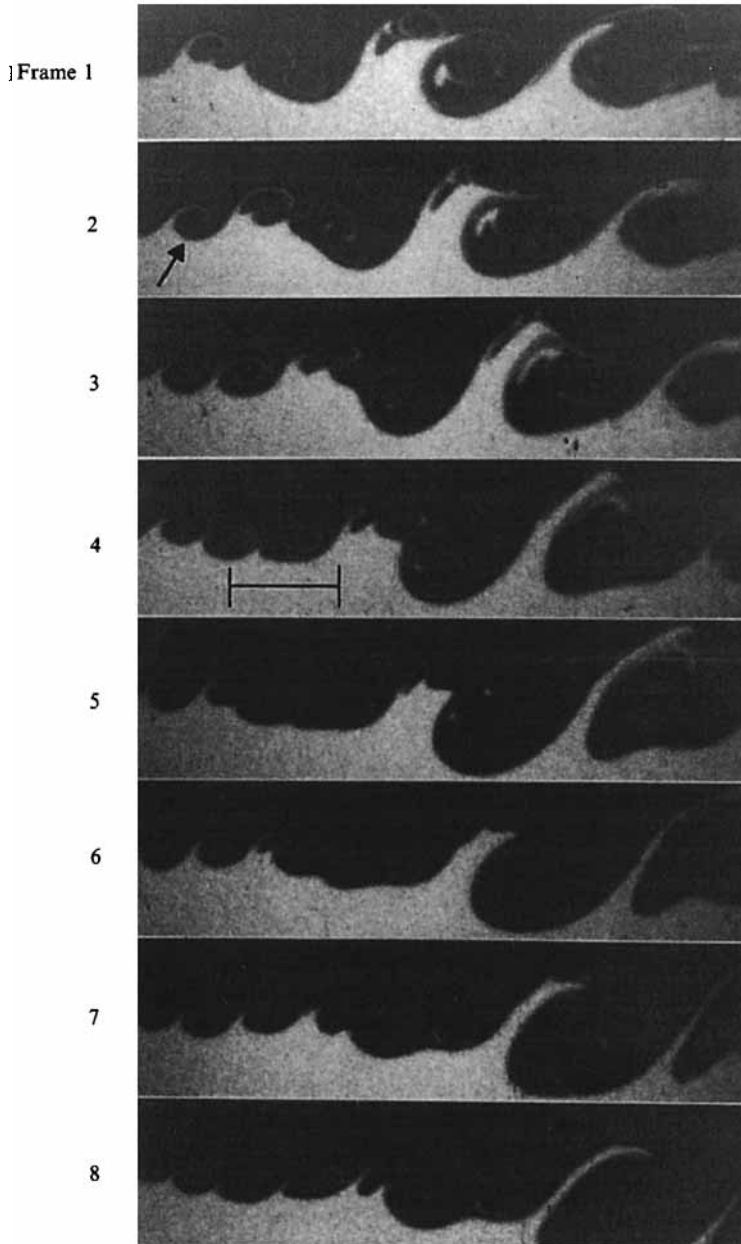


FIGURE 3. A flow visualization sequence of the shear layer at $U_1 = 1.8$ m/s, $U_2 = 0.9$ m/s. The lower/slow stream contains silicone oil aerosol. The range within which vortices were sampled, for the ensemble-average measurements, is shown in frame 4. Time lapse between frames is 20 ms.

also pre-eminently apparent as a broad peak in the spectrum of the velocity fluctuations. The average vortex spacing was found to be $\lambda_0 = 3.0$ cm which is a good estimate of the initial (or most unstable) wavelength. Thus, a convection velocity of 1.35 m/s is suggested, which is equal to the arithmetic mean of the two free-stream velocities. This was also observed by direct measurement of the convection velocity, by measuring the relative displacement of a vortex between successive frames. For

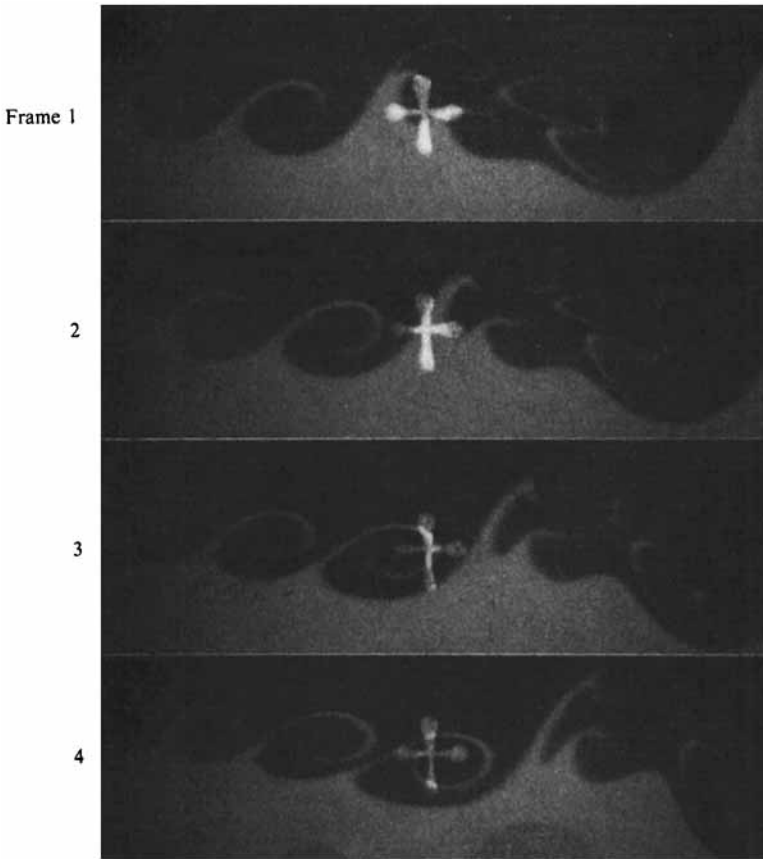


FIGURE 4. A flow visualization sequence, simultaneously obtained with LDV measurements. Both streams are seeded with silicone oil aerosol. The LDV probe volume is at $x = 17.8$ cm ($5.9\lambda_0$), $y = 0$. Time lapse between frames is 10 ms.

a sample of 612 passive (i.e. not in the process of interacting) vortices, spanning several generations (i.e. including vortices formed through coalescence events), an average value of 0.49 was obtained for $U_c/(U_1 + U_2)$ with a standard deviation of 0.034. Thus, as long as a vortex is passively convecting downstream, its speed is well approximated by the arithmetic mean of the two free-stream velocities.

Figure 4 shows a flow visualization sequence, obtained with simultaneous LDV velocity data. It should be noted that the region covered in this sequence (15 cm in the streamwise direction) is approximately the left half of that shown in figure 3. Two films were used for data analysis, one for which the point of velocity measurement is $x = 17.8$ cm ($5.9\lambda_0$) downstream of the splitter-plate trailing edge, and the other at $x = 20.3$ cm ($6.8\lambda_0$). Each film contains 7 runs each corresponding to a different transverse location of the point of velocity measurement. A stop-motion projector was used to project the film onto a screen comprising the sensitive area of an acoustic digitizer, interfaced with a PDP 11/23 microcomputer, used to obtain and record spatial information. Each run, containing approximately 380 frames was processed separately using the following procedure. Starting from the first frame (i.e. that for which the LED's were lit; see §3.1), subsequent frames were projected onto the screen until, nearest to the point of velocity measurement, an eligible vortex was

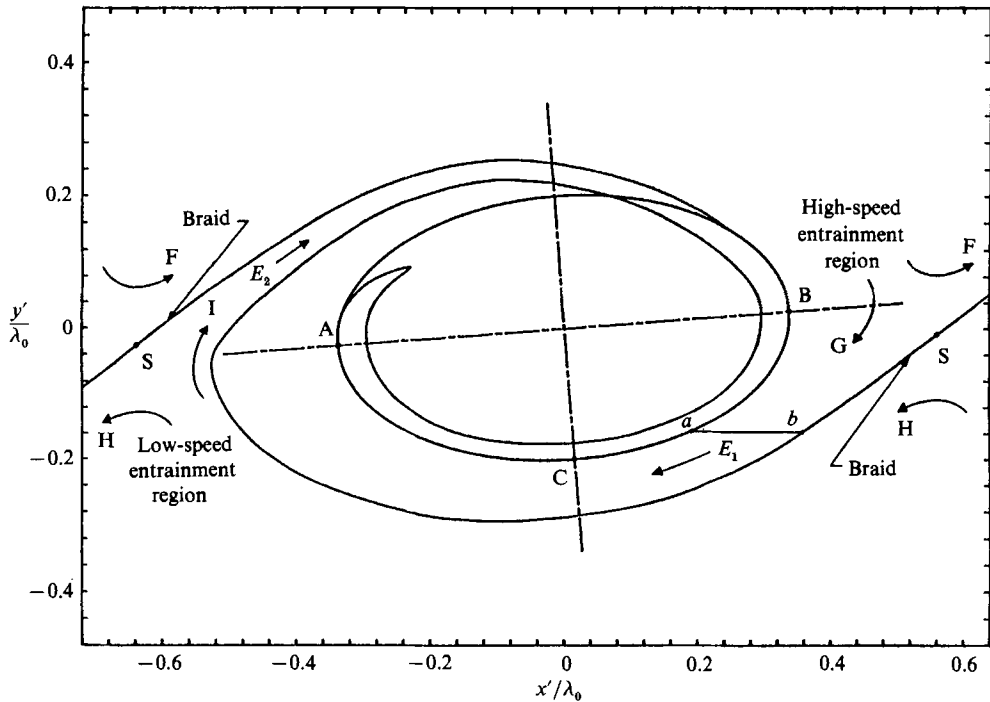


FIGURE 5. A typical eligible first generation vortex whose core coincides with that of the average vortex.

observed. A first generation vortex qualified so long as it did not, or was not about to, participate in a coalescence event and was sufficiently but not over-developed. The schematic of figure 5 elucidates the latter stipulation; that is, a vortex was considered if its cusp was above the line AB as shown. The reasons for this is that for vortices observed within a narrow range of streamwise locations, the amount of rollup of the cusp is a reflection of the vorticity contained within them. Therefore, those which were too weak or too strong (this being a manifestation of the irregularity in their formation), were rejected. Only passive, first generation vortices of approximately the same age and strength were consequently considered.

A total of 1552 vortices were sampled (from the analysis of the same number of frames), for each one of which the following information was recorded: the frame number, the dimensions and orientation of the ellipse which best fits the vortex core, and the coordinates of the ellipse centre relative to the point of velocity measurement. The procedure for vortex identification is illustrated in figure 5, points A and B, which determined the major axis dimension and the orientation of the representing ellipse, were readily identifiable; as for point C, however, it was necessary to identify several points (typically 5–10) along the lower portion of the vortex core and then, through a least-square-fit analysis, determine the dimension of the minor axis. The average and standard deviation of the major and minor axis dimensions over all samples, are $a/\lambda_0 = 0.35 \pm 0.041$ and $b/\lambda_0 = 0.20 \pm 0.023$ respectively; moreover, $a/b = 1.75 \pm 0.19$ and the orientation $\theta = 4.5^\circ \pm 3.8^\circ$. It is interesting to note that the average values are in good agreement with those of Hernan & Jimenez (1982) obtained in a high-Reynolds-number shear layer. For example, they found $a/b = 1.92 \pm 0.67$ and $\theta = -4.5^\circ \pm 17.0^\circ$. The greater dispersion of their results is because

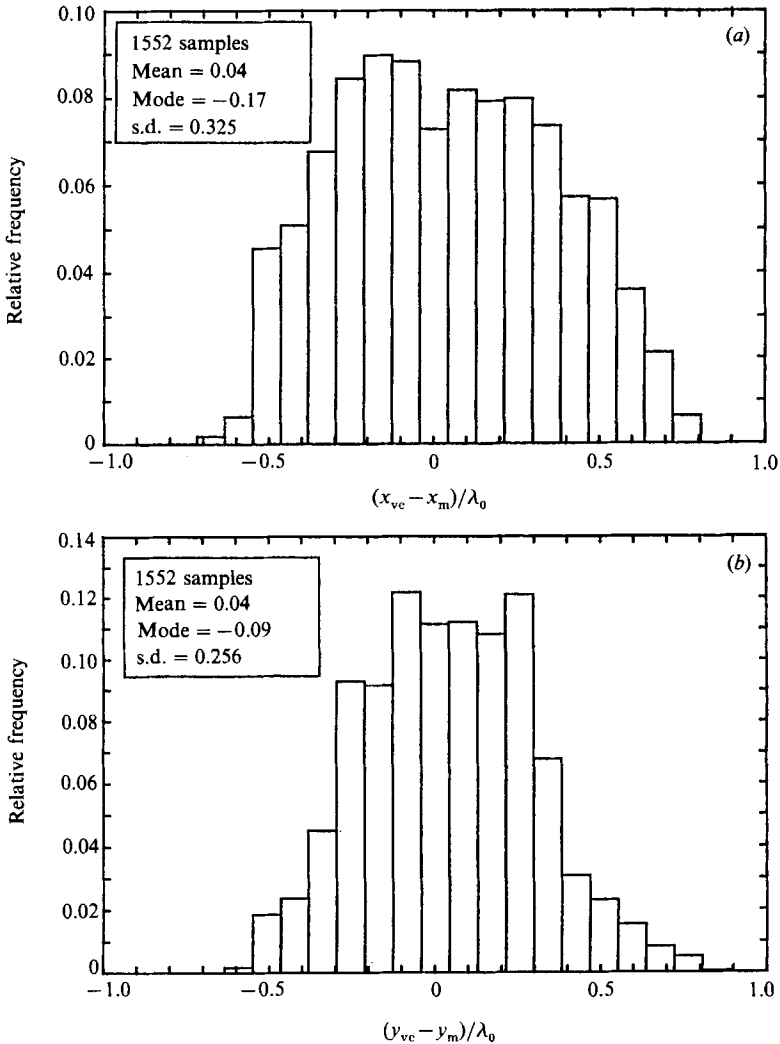


FIGURE 6. Frequency distribution histogram of (a) $(x_{vc} - x_m)/\lambda_0$, (b) $(y_{vc} - y_m)/\lambda_0$.

they sampled vortices over a much wider range of streamwise locations, spanning several vortex generations.

The ellipse having the average dimensions and orientation is actually shown in figure 5 along with a vortex (overlaid by projecting a ciné film) representing the average of all sampled vortices, whose core it circumscribes. Note that x' and y' are the streamwise and transverse coordinates relative to the ellipse centre. If, for a given frame (or vortex) the coordinates of the ellipse centre are x_{vc} , y_{vc} and those of the point of velocity measurement are x_m , y_m then, the spatial distributions of $x_{vc} - x_m$ and $y_{vc} - y_m$ over all analysed frames (or sampled vortices) are shown in figures 6(a) and 6(b) respectively. The larger dispersion in figure 6(a) is because the streamwise range within which vortices were selected is greater than their lateral deviation. Although not uniformly distributed, most vortices were sampled within a streamwise extent of about λ_0 and a lateral extent slightly less than λ_0 , relative to the point of velocity measurement. The average x_{vc} is $6.2\lambda_0$, the streamwise station to which the results will be referred. The average y_{vc} is $0.092\lambda_0$, slightly below (i.e.

$-0.025\lambda_0$) the local transverse location at which $\langle U \rangle = \frac{1}{2}(U_1 + U_2)$; this is consistent with the results of Koochesfahani *et al.* (1979).

The data thus extracted from the various runs of the two flow visualization movies were then used to condition the velocity data of the corresponding data files, the link between the two records being the frame number. Since the data was acquired at a rate of 2 kHz (i.e. 0.5 ms between successive samples), during the time the shutter was open (i.e. $1/600$ s = 1.67 ms), three data points were acquired. With at most an error of 0.5 ms, it was assumed that the visual data were obtained at the midpoint of the exposure time. Invoking Taylor's hypothesis, a spatial description was inferred for 19 successive measurements (over a time interval of 9 ms), the midpoint of which coincided with that of the exposure time. In other words, it was assumed that for 9 ms the vortex remained stationary, while the measurement point moved towards the negative streamwise direction with a constant speed U_C (the convection velocity), surveying the two velocity components once ever 0.5 ms. For each vortex then, the streamwise and transverse velocity components were obtained at 19 locations, the coordinates of which, relative to the ellipse (circumscribing the vortex core) centre, were

$$(x_m - x_{vc}) - i\Delta x, (y_m - y_{vc}) \quad \text{for } i = -9 \text{ to } 9,$$

where $\Delta x = U_C \Delta t = 0.675$ mm or $0.0225\lambda_0$ with $\Delta t = 0.5$ ms and $U_C = 1.32$ ms. In all, velocity measurements at 29500 points, distributed about the average vortex core, were obtained. These were stored in one datafile, which served as the database for the ensemble-average velocity computations.

It is clear that the crucial step of the data analysis is the conversion of temporal data to a spatial distribution through Taylor's hypothesis. Zaman & Hussain (1981), who considered in detail the applicability of Taylor's hypothesis to large-scale coherent structures, found that it works well in the case of a passive vortex, using a constant convection velocity. It was noted earlier that a small dispersion in the measured convection velocity was observed (see figure 4); thus, the assumption that all eligible vortices travelled with the same convection velocity (i.e. $U_C = 1.32$ ms), appears to be quite reasonable. It should also be noted that the extent over which Taylor's hypothesis is applied here, is but a fraction of the vortex spacing since, in 9 ms, the displacement of the vortex is $0.45\lambda_0$. The assumption, figuratively stated as the vortex remaining stationary for 9 ms, also implies that during this time the identifying features of the vortex core remain unaltered (i.e. the vortex is 'frozen'). This was confirmed by direct flow visualization; other than translation and a slight rollup of its cusp, the same vortex, between two successive frames (i.e. a time lapse of 10 ms), retained its core features.

4. Results and discussion

As was noted in the previous section, the end result of the data processing was measurements of the streamwise and transverse velocity components at a large number of points, non-uniformly distributed about the average vortex core. The spatial distribution of these can be inferred from figures 6(a) and 6(b). To obtain ensemble averages, the coordinate frame of the average vortex core was discretized into a 31×21 grid network, using a grid size of 1.25×1.25 mm or $0.042\lambda_0 \times 0.042\lambda_0$. Local averages of both velocity components, ascribed to the geometric centre of the grid, were then computed based on the ensemble of measurements within each grid.

The resulting spatial distribution of the ensemble-average velocity is shown in figure 7. At each grid the magnitude and direction of the vector are determined by

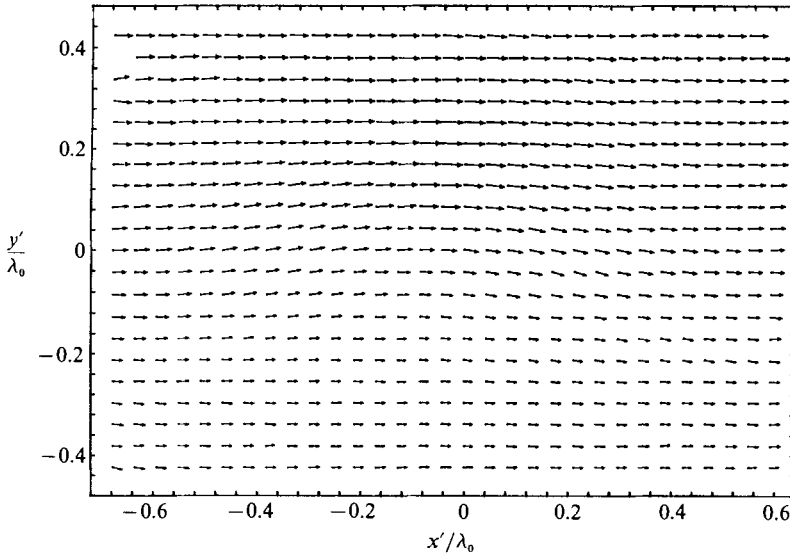


FIGURE 7. Ensemble-average velocity field in a fixed frame of reference.

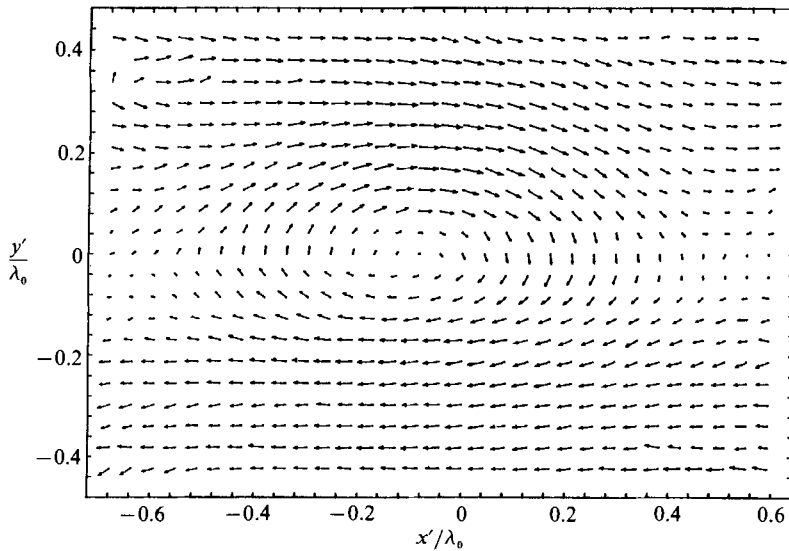


FIGURE 8. Ensemble-average velocity field in a frame of reference moving with the vortex convection velocity.

the two ensemble-average velocity components, its origin is at the geometric grid centre. The velocity field shown in figure 7, however, does not show any signs of vortical motion. In a reference frame moving with the vortex (i.e. $U_c = 1.32$ m/s) though, a very different picture emerges. This is shown in figure 8, obtained by subtracting U_c from the streamwise component of the velocity vectors of figure 7; the resulting velocity field is clearly that expected of a vortex since a region of high circulation is unmistakably apparent. The centre of this region, or more appropriately the vortex centre, is situated near the origin (i.e. the centre of the average vortex core). Also noteworthy are the stagnation points near the left and right sides of the figure. These have been previously observed by Dimotakis (1986) and their

topological necessity was mentioned by Coles (1981). A more detailed discussion of the flow field shown in figure 8 will follow, but first, it is necessary to consider the accuracy of these results.

The non-uniform spatial distribution of the measurements results in fewer samples for grids far from the vortex core. It is for this reason that at the corners of figure 8 (i.e. for grids farthest from the origin) statistically converging averages were not obtained; in fact, the 'blanks' at the top two corners are the result of having no samples within these grids. On the other hand, near the origin, ensemble averages from as many as 150–200 samples were determined. Next, it should be noted that ensemble averaging filters out the random component of the instantaneous velocity which is primarily the result of small random measurement errors (such as, for example, the discretization error of the LDV counters). This occurs even for infinitesimally small grids; however, by averaging over a finite area, the velocity is, in effect, low pass filtered at a cutoff frequency inversely proportional to the grid size. For the discretization used to obtain figures 7 and 8, this results in a cutoff frequency of about 1 kHz, that at which the analog LDV signals were low pass filtered (see §2.2). Moreover, the selected grid size is small enough to be able to capture the largest spatial gradients (estimated from instantaneous velocity traces). The velocity field shown in figure 8, to within the limitations of statistical ensemble averaging, therefore represents the coherent (i.e. non-random) motion induced by the average (of all samples) vortex. Errors in obtaining (i.e. digitizing, finite exposure time, etc.) and deducing (i.e. Taylor's hypothesis) a spatial description are estimated to result in an overall uncertainty of about $\pm 0.04\lambda_0$.

4.1. Vortex flow field and entrainment

The results of figures 5 and 8 are summarized in figure 9 obtained by superposition. It will be recalled (see §3.2) that the vortex shown in figure 5 (and figure 9) is representative of the ensemble used to obtain these results. Since its core coincides with that of the average vortex, the superimposed ensemble-average velocity field should best approximate its instantaneous velocity field. With this viewpoint, namely that figure 9 is an instantaneous picture, several observations can be made, for which it will also be necessary to refer to figure 5.

The interface shown in figures 5 and 9 separates the initially low- and high-speed free-stream fluids which, in a reference frame translating with the vortex (as is the case in figure 9), appear to travel in opposite directions. Note that the interface spirals around the vortex (see figure 9); it is, in fact, for this reason that the centre of the ellipse, defined by the interface points, A, B and C (see figure 5) and defining the vortex core, lies to the right of the vortex centre.

Entrainment of free-stream, initially low-speed fluid takes place on the trailing side of the vortex. First, it is drawn towards the low-speed entrainment region (see figure 5). Then the fluid nearest to the vortex is engulfed by it, as it follows a path leading to the vortex core. This is schematically shown in figure 5, where arrow I denotes the path and E_2 the entrainment flux of the initially low-speed fluid. However, not all of the fluid drawn towards the low-speed entrainment region ends up in the vortex. That which is farthest from it, or nearest to its preceding neighbour, follows an opposite path (i.e. path HY in figure 5) towards, but not inwards, the latter. This can be seen by considering the fluid originating from the low-speed entrainment region of the preceding (the one shown in figures 5 and 9) vortex, i.e. path H on the right side of figure 5. More or less the same sequence of events is observed for the entrainment of free-stream, initially high-speed fluid which,

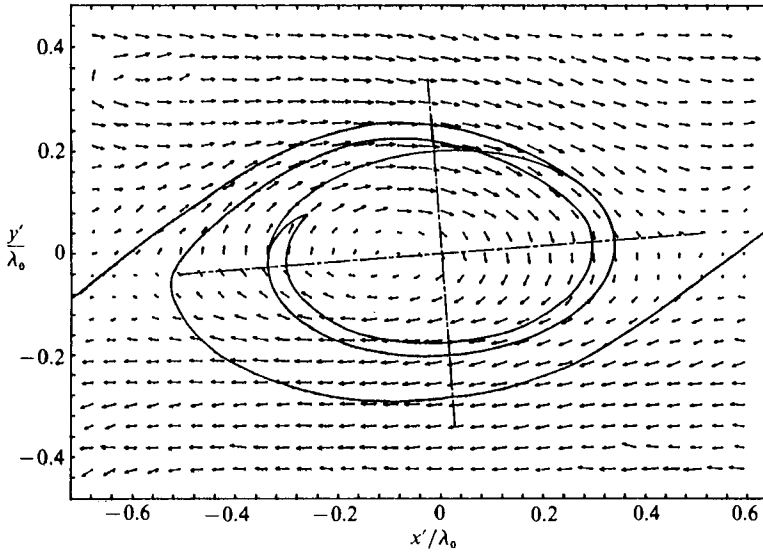


FIGURE 9. Superposition of figures 5 and 8.

however, occurs at the leading side of the vortex. Fluid drawn towards the high-speed entrainment region, depending on which vortex it is nearest to, follows one of two paths: one (path G) by which it is led around the lower perimeter of, and eventually into, the vortex core (the entrainment flux being E_1), and the other (path F) whereby it is directed towards the preceding vortex. The entrainment regions of two adjacent vortices are separated by the braid (i.e. that portion of the interface which connects them). This is so because it passes through the stagnation point (point S in figure 5) which is the result of the rotation of the two, neighbouring, like-signed vortices. In the near vicinity of the stagnation point (also referred to as the saddle point), the braid is nearly straight and oriented along a direction 45° relative to the streamwise direction. Locally, the flow on either side of the braid is reminiscent of a stagnation point flow. Unentrained high-speed fluid (following path F) and entrained low-speed fluid (following path I), separated by the braid, move towards the leading vortex. On the other side (of the stagnation point), entrained high-speed fluid (following path G) and unentrained low-speed fluid (following path H) move towards the preceding vortex. Thus, the intervening region between two neighbouring vortices is characterized by a straining field aligned with the braid which, as a result, is continually being stretched, the largest strain occurring at the saddle point.

Continuing with the notion that figure 9 represents a 'snapshot' of a vortex superimposed onto an ensemble-averaged associated velocity field, it is interesting to examine its evolution, presuming it remains passive. To this end, insight is gained by following the first vortex of the second frame, in the flow visualization sequence of figure 3. Note that between the fourth and fifth frames, the vortex appears to disconnect from the low-speed side, as entrainment of low-speed fluid into its core ceases quite abruptly. A close-up view of a 'detached' vortex is shown in figure 10; it may be seen that the vortex is not actually disconnected but that, rather, the path adjacent to the braid (through which low-speed fluid is entrained) is stretched to the point where it is barely visible. The low-speed entrainment region is now occupied by a 'pocket' of entrained, formerly high-speed, fluid which, under the action of the

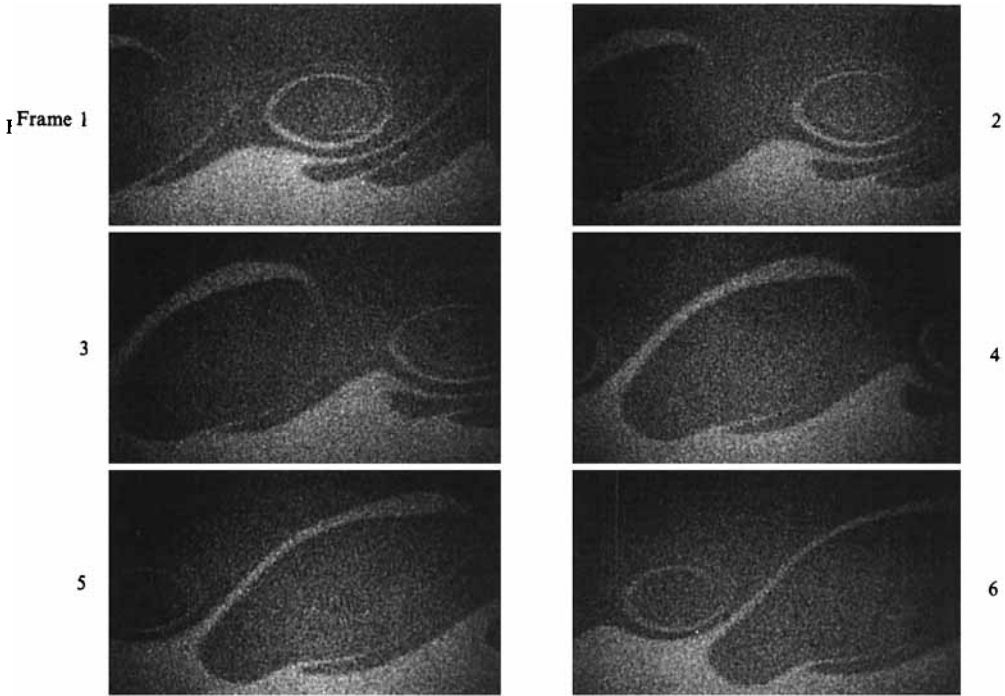


FIGURE 10. A flow visualization sequence showing 'close-up' a first generation vortex, detached from the low-speed side. Time lapse between frames is 10 ms.

neighbouring vortex, moves backwards (see figures 10 and 3). Thus, while the vortex continues to entrain high-speed fluid, most of it is diverted towards the pocket instead of the core which is seen primarily to elongate rather than enlarge (see figure 3). A more detailed discussion is given by Panides (1987) who, through extensive observation of flow visualization sequences and limited measurements of the entrainment flux (e.g. E_1 and E_2 in figure 5), found that entrainment of low-speed fluid is a highly discontinuous process occurring in brief 'spurts', while from the high-speed side, entrainment is more of a continuous, quasi-steady mechanism; this, he also observed for second and third generation vortices (i.e. vortices formed through coalescence events), accounting for a large entrainment asymmetry in the shear layer, which favours the high-speed side. In light of this discussion, returning to figure 9, it may be seen that the interface next to the low-speed entrainment region does show the tendency to move back and form a pocket where entrained high-speed fluid later accumulates. Observation shows that pocket formation and vortex detachment occurs on a timescale which is small in comparison to the mean vortex lifetime; the moment it occurs is usually after complete rollup (i.e. when the cusp is beyond point A as shown in figure 5), but the exact time is apparently a function of the size, strength and disposition of the neighbouring vortices (Panides 1987). Thus, the vortex shown in figures 5 and 9 is one of the 'pocketless' vortices that were sampled; the ensemble though, did include vortices with a substantially different interface topography in the low-speed entrainment region (e.g. see figures 3 and 4).

By measuring the evolution of the normalized aerosol concentration profiles across the shear layer, Panides (1987) found an average entrainment ratio of 1.5, favouring the high-speed side. This is greater than 1.23, which is the value predicted by the

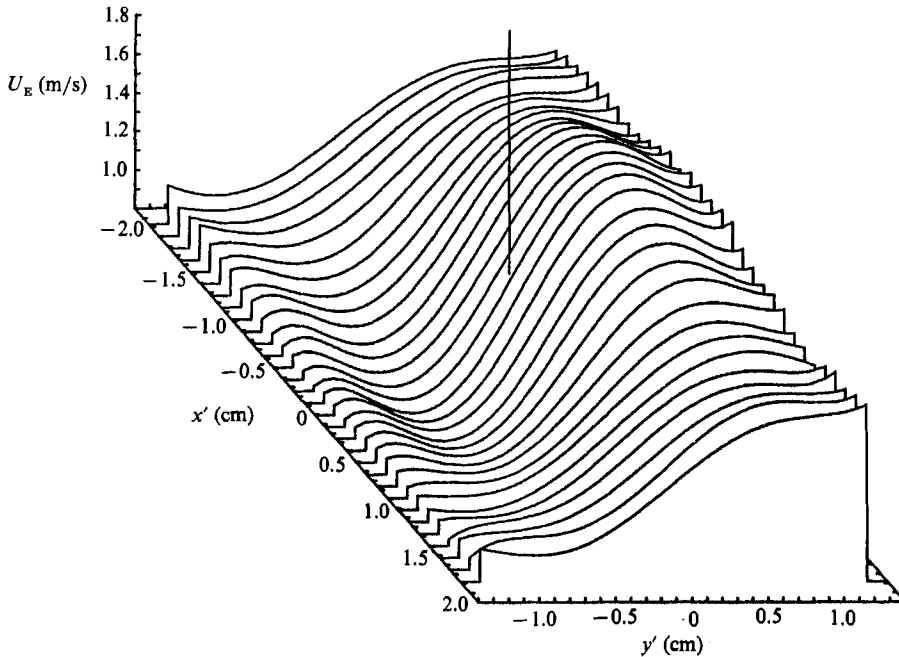
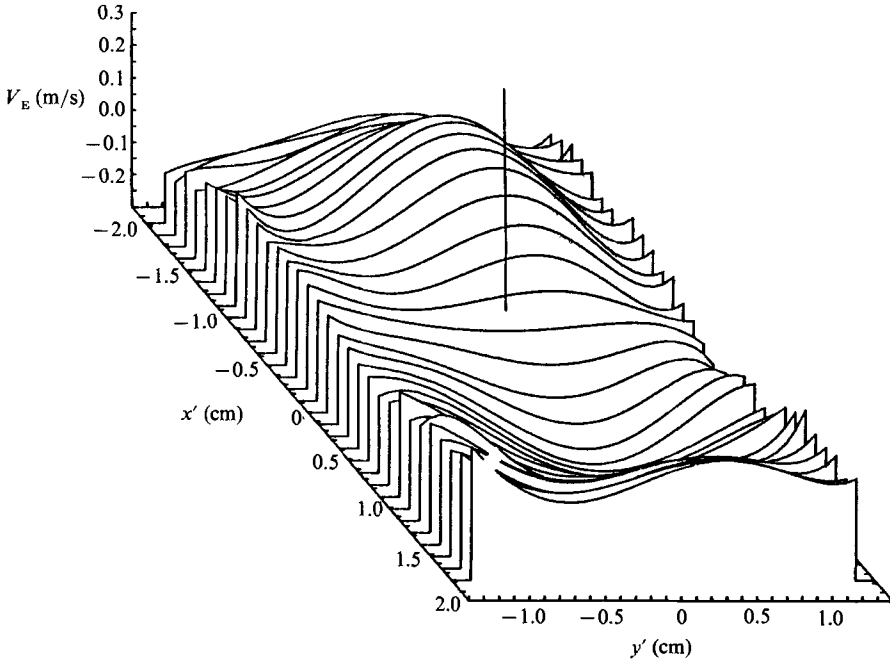


FIGURE 11. Variation of $U_E(y')$ along x' .

empirical model of Dimotakis (1986), for a free-stream speed ratio $U_2/U_1 = 0.5$. Closely examining the visualization sequences (e.g. figures 3, 4 and 10), however, it is clear that the entrainment asymmetry is far greater than is suggested by either of these values. The reason for this stems from the fact that, typically, computing the average entrainment ratio amounts to an integration within arbitrary shear layer boundaries (Panides 1987; Konrad 1976). Thus, for the reasons discussed in the previous paragraph, the instantaneous local entrainment ratio undergoes large temporal variations, and can assume values much greater than the average. These observations are consistent with those of Roberts (1985).

4.2. Average vorticity distribution

The obtained ensemble-average velocity data consist of the 31×21 (i.e. 651 grids) arrays $U_E(x', y')$ and $V_E(x', y')$, where x' , y' are the coordinates of the grid centre, relative to the centre of the average vortex core, and the subscript E denotes an ensemble-average quantity. Smooth profiles of $U_E(y')$ and $V_E(y')$ along constant x' values were obtained by sorting out the 31 columns of each one of the two data arrays, and then fitting (in a least-square sense) a fifth-order polynomial through the 21 elements of each column. The results for U_E and V_E are shown in the three-dimensional plots of figures 11 and 12 respectively. In these figures the line emanating from the surface (parallel to the U_E , V_E axes), identifies the position of the vortex centre as suggested by figure 8. A comparison clearly illustrates the inherent differences in the vortex-induced fluctuations between the two velocity components. That is, relative to the x' axis (i.e. $y' = 0$) the $V_E(y')$ profiles are symmetric, whereas the $U_E(y')$ profiles are antisymmetric with respect to the velocity of the vortex centre (i.e. the convection velocity). On the other hand, it can be inferred (from figures 11 and 12) that the $U_E(x')$ and $V_E(x')$ profiles have exactly the opposite properties relative to the y' axis.

FIGURE 12. Variation of $V_E(y')$ along x' .

From the ensemble-average velocity data the z -component of the vorticity was computed according to

$$\omega(x', y') = \frac{\partial}{\partial y'} U_E(x', y') - \frac{\partial}{\partial x'} V_E(x', y').$$

At each grid centre the derivatives were determined by differentiating the polynomials representing the $U_E(y')$ and $V_E(x')$ profiles. In this manner, a 31×21 array for the vorticity field was obtained. The maximum value of the vorticity is $\omega_{\max} = 197 \text{ s}^{-1} = 6.1\Delta U/\lambda_0$ occurring at $x' = 0.06\lambda_0$, $y' = 0.02\lambda_0$. Contours of constant vorticity, normalized by the peak value (i.e. ω/ω_{\max}), are shown in figure 13. Before discussing these results, it should be noted that this figure can only be interpreted in the context of an average representation, the reason being that the instantaneous vorticity exhibits an intricate and ever-changing pattern of folds between vortical and irrotational fluid, which is difficult to resolve with any averaging technique. In this case a true global velocity – better yet, vorticity (since differentiation of experimental data, generally a noise producing process, is avoided) – measuring technique is required.

Returning to figure 13, evidently the (average) first generation vortex is characterized by a uniform in space, yet non-uniform in magnitude, vorticity distribution of an elliptical cross-section. The contours of constant velocity at regular increments are approximately concentric about the vortex centre. As such, from the peak value at the vortex centre, the vorticity drops symmetrically along the lateral extent of the vortex, faster than it does along its streamwise extent. Interestingly, this field has many of the attributes of the theoretical distribution given by Stuart (1967); the best agreement appears to be for a vorticity concentration parameter of about 0.4 (note that a value of 0 corresponds to a uniform distribution and 1 to a point vortex). Browand & Weidman (1976), through ensemble averaging, obtained

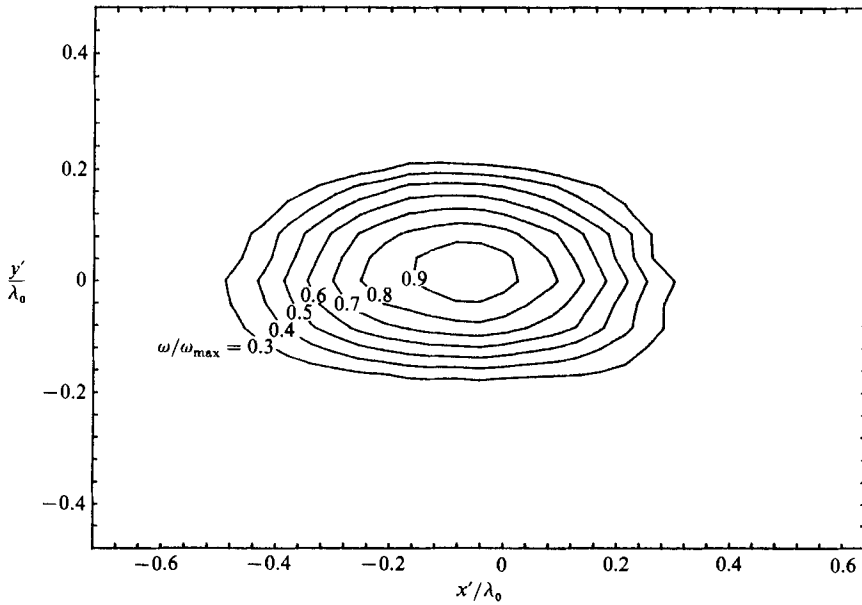


FIGURE 13. Contours of constant vorticity for the average vortex.

the average vorticity distribution of a newly formed second generation vortex (i.e. just after the coalescence event leading to its formation). In comparing their results to the Stuart vortex, they noted that the measured distribution was broader in the lateral direction than for any theoretical distribution while, along the longitudinal direction, best overall agreement was obtained for a vorticity concentration parameter of 0.25. Thus, a direct comparison between their results and those presented here suggests that coalescence leads to (second generation) vortices exhibiting a more uniform (in magnitude) vorticity distribution, which is consistent with the results of Zaman & Hussain (1980). It should also be noted that an elliptical vorticity distribution, along with a small inclination angle (i.e. $\theta = 4.5^\circ \pm 3.8^\circ$), confirm the conjectures of Koochesfahani *et al.* (1979) and the stability analysis of Moore & Saffman (1975), for a passive vortex.

Note that in figure 13, the lowest value of the vorticity that is indicated is $\omega/\omega_{\max} = 0.3$. The reason for this is that the uncertainty, on the basis of irrotational flow in the free streams, is estimated to be about $\pm 0.1\omega_{\max}$. It is interesting to note then that, within the accuracy of the measurement, the (average) vortical region does not include the interconnecting braid between adjacent vortices (see figure 5; compare with 13) which has little or no circulation association with it. Thus, at this stage in the life of the vortex (i.e. $6.2\lambda_0$ downstream of the splitter-plate trailing edge), most of the vorticity has migrated to the core, with the braid having been essentially depleted of its vorticity.

4.3. Zone-average statistics

At a particular lateral location y' , the zone-average streamwise velocity U_Z is obtained from the corresponding $U_E(x')$ profile as

$$U_Z = \frac{1}{(x'_2 - x'_1)} \int_{x'_2}^{x'_1} U_E(x') dx', \quad (1)$$

where $x'_1 = -0.64\lambda_0$ and $x'_2 = 0.56\lambda_0$ are the streamwise coordinates (relative to the centre of the average vortex core) of the stagnation points on the trailing and leading sides of the vortex, respectively. These values were obtained from figure 8 (see also figure 9) and by examining the periodicity of the $V_E/(x')$ profiles, since these appear very nearly periodic with an 'average' wavelength of $x'_2 - x'_1 = 1.2\lambda_0$. The implication of a greater (by 20%) vortex spacing is a reflection of the fact that many of the sampled vortices had neighbours in the process of merging. In such cases, the coalescing vortex moved away from the one being sampled, so that the distance between the latter's centre and their stagnation point was greater than $0.5\lambda_0$ (as would, on the average, be the case if both vortices were passive). This could have been avoided simply by rejecting vortices with such neighbours. However, such a stipulation would have significantly reduced the number of samples since, in the region where they were sampled, a sequence of three passive vortices was rarely observed.

Thus, U_Z , as defined by (1) represents the effect of a single (the average) first generation vortex. Another perspective is gained by, once again, invoking Taylor's hypothesis, this time to convert a spatial distribution to temporal data. That is, by replacing x with $U_C t$ in (1), U_Z then represents the time-average velocity, owing to the passage of a single vortex, past a stationary measurement point; the averaging time therefore corresponds to one period, equal to $(x'_2 - x'_1)/U_C = 1.2\lambda_0/U_C$. For that matter, so long as the averaging time is an integer number of periods, U_Z can also be considered as the long-time average, owing to the passage of the same number of identical (in strength, spacing, position, etc.) first generation vortices. This, for example, would very nearly be the case in a forced shear layer, where variations in the vortex characteristics are substantially reduced. With this viewpoint, it is interesting then to compare zone-average statistics with conventional time-averaged quantities. First, it will be necessary to define the zone-average streamwise and transverse r.m.s. fluctuations u_Z and v_Z respectively, from

$$u_Z^2 = \frac{1}{(x'_2 - x'_1)} \int_{x'_1}^{x'_2} [U_E(x') - U_Z]^2 dx' \tag{2}$$

and

$$v_Z^2 = \frac{1}{(x'_2 - x'_1)} \int_{x'_1}^{x'_2} [V_E(x') - V_Z]^2 dx'. \tag{3}$$

Also, the zone-average Reynolds stress $-(uv)_Z$ is defined as

$$-(uv)_Z = \frac{1}{(x'_2 - x'_1)} \int_{x'_1}^{x'_2} [U_E(x') - U_Z][V_E(x') - V_Z] dx'. \tag{4}$$

Using (1)–(4), U_Z , u_Z , v_Z and $-(uv)_Z$ were computed for each of the 21 lateral positions (relative to the average vortex, as suggested by figure 8), from the corresponding $U_E(x')$ and $V_E(x')$ profiles. The resulting zone-average profiles $U_Z(y')$, $u_Z(y')$, $v_Z(y')$, and $-(uv)_Z(y')$ are shown in figures 14, 15, 16 and 17 respectively, along with the corresponding time-average profiles, $\langle U \rangle(y')$, $u'(y')$, $v'(y')$, and $-\langle uv \rangle(y')$ obtained at $x = 5.1\lambda_0$ where all of the passing vortices belonged to the first generation. However, owing to the irregularity in their formation, there were variations in the size, strength, position, etc. of the vortices; moreover, several of them were laterally displaced in assuming the early stages of a coalescence interaction (see below). This comparison is therefore aimed at revealing the effect of these variations (which are effectively filtered out with zone-average statistics) on the time-averaged profiles. It

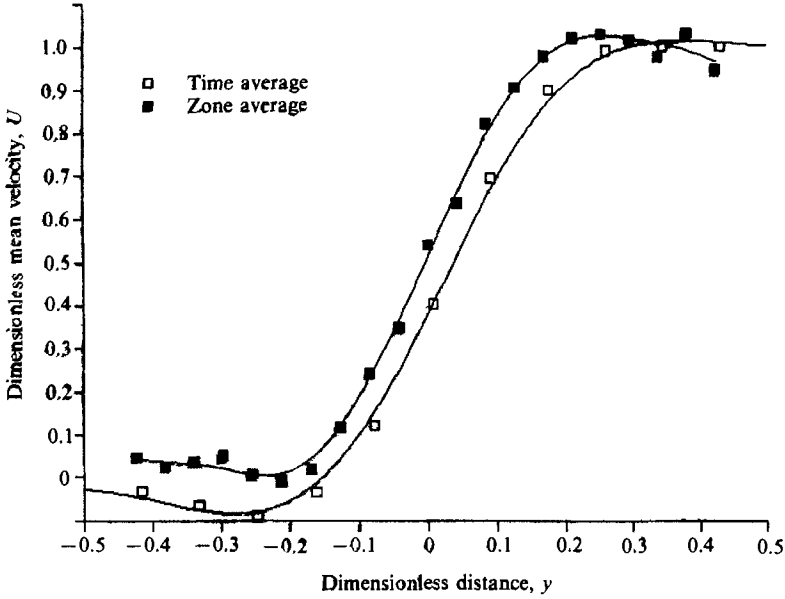


FIGURE 14. $[\langle U \rangle(y') - U_z]/\Delta U$ and $[U_z(y') - U_z]/\Delta U$ vs. y'/λ_0 .

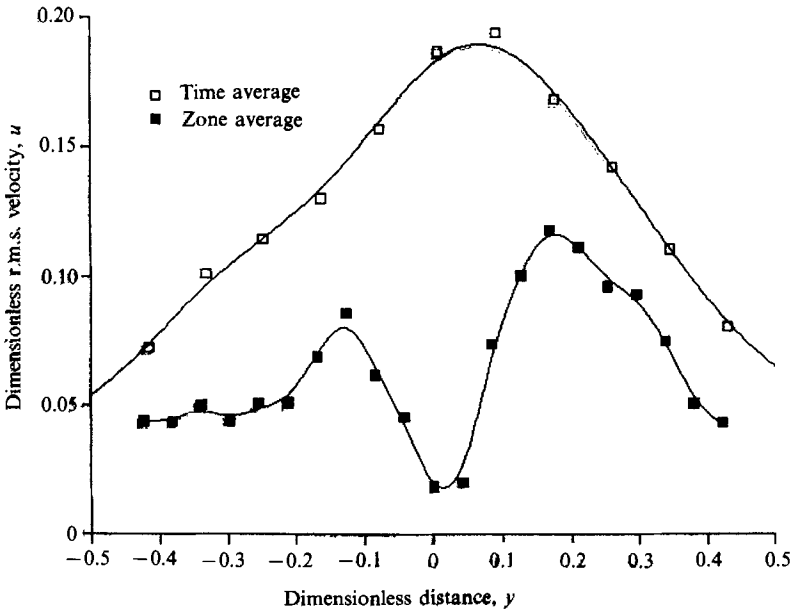


FIGURE 15. $u'(y')/\Delta U$ and $u_z(y')/\Delta U$ vs. y'/λ_0 .

should be noted that the abscissa scaling in figures 14–17 is y'/λ_0 where, for the time-averaged profiles, the relation $\langle y_{vc} \rangle = 0.092\lambda_0 \rightarrow y = y' + 0.092\lambda_0$ (i.e. the centre of the average vortex core is $0.092\lambda_0$ above the trailing edge of the splitter plate) has been used.

Figure 14 shows that U_z is quite similar to U except that U appears slightly broader or, conversely, U_z displays a slightly steeper slope. That the time-average profiles are broader is clearly evident in figure 15, which shows the streamwise r.m.s.

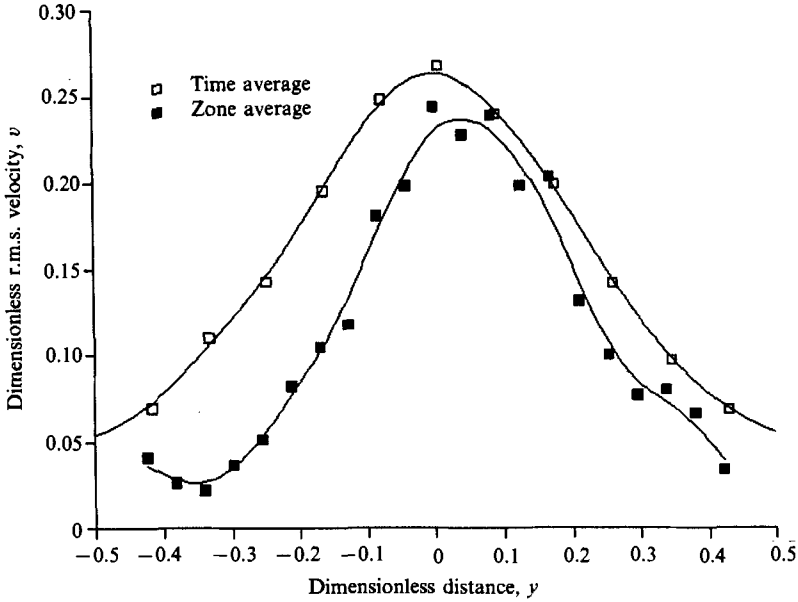


FIGURE 16. $v'(y')/\Delta U$ and $v_z(y')/\Delta U$ vs. y'/λ_0 .

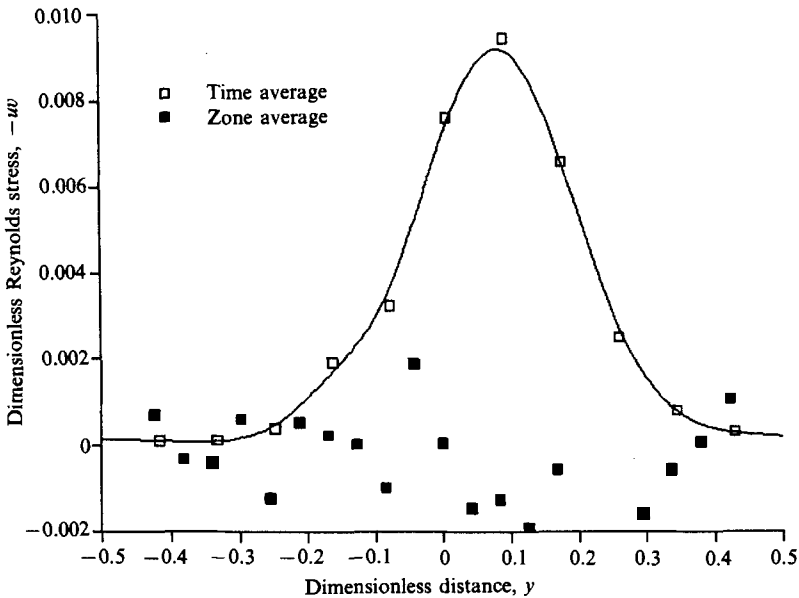


FIGURE 17. $-\langle uv \rangle(y')/\Delta U^2$ and $-(uv)_z(y')/\Delta U^2$ vs. y'/λ_0 .

fluctuations. However, most interesting is that the character of u' and u_z is strikingly different; that is, u_z attains peak values symmetrically situated about the vortex centre (i.e. $y' = 0.02\lambda_0$; see §4.2) whereas, at the vortex centre, it is very nearly zero. On the other hand, u' displays a single peak whose value ($0.19\Delta U$) exceeds those of both U_z peaks ($0.09\Delta U$ and $0.12\Delta U$ on the low- and high-speed sides respectively). The results for u_z , however, represent the effect of a single vortex or, as was noted earlier, a series of aligned (in the streamwise direction) identical such vortices. When the measurement point coincides with the vortex centre(s) (i.e. $y_m = y_{vc} = 0$), no

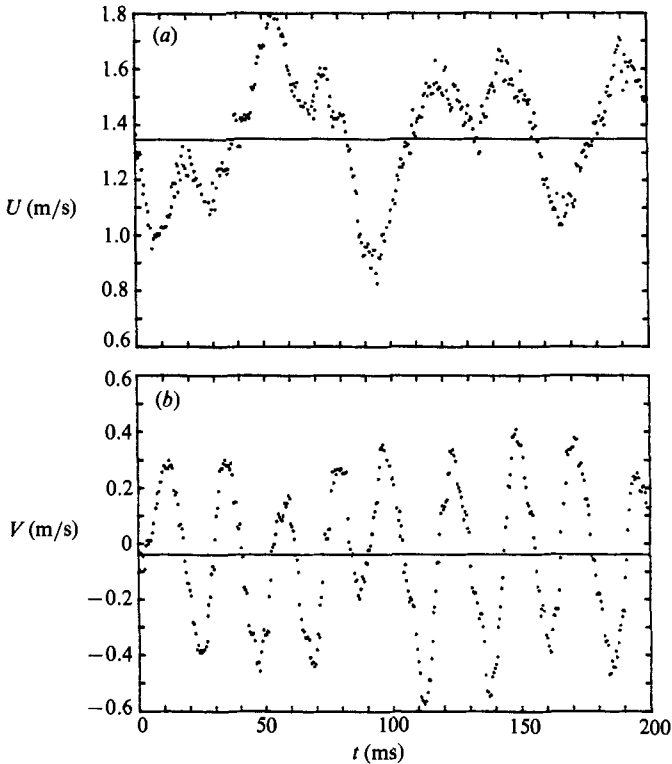


FIGURE 18. Time trace of the two velocity components (a) $U(t)$, (b) $V(t)$; $x = 15.24$ cm ($5.1\lambda_0$), $y = 0$.

streamwise fluctuations are induced. On the other hand, owing to the large lateral gradient in the mean velocity (see figure 14), the smallest of variation in $y_m - y_{vc}$ between successive vortex passages results in significant streamwise fluctuations; these are largest when, in a sequence of two vortices, $y_m - y_{vc}$ switches sign (i.e. one vortex passes above the measurement point, and the next one below it or vice versa). This can be seen in figure 18 which shows velocity traces obtained at $x = 5.1\lambda_0$, $y = 0$ along with the average values (over the total time record), indicated as the straight lines at $U = 1.35$ m/s and $V = 0.04$ m/s. Note that the passage of nine vortices can clearly be inferred from V (see figure 18b). From the U -velocity trace (figure 18a) it can be seen that the centres of the first two vortices were below the measurement point, while the next two were above and so on; the large fluctuation about the mean during this transition is clear. Thus, these fluctuations contribute most to u' in the vicinity of the (unforced) shear layer centre. As a result, the profile of u' has a single peak, the position of which identifies the most probable location for this random process (i.e. $y_m - y_{vc}$ changing sign), and the associated large fluctuations, to occur. Moreover, the magnitude of the u' peak is greater than either of the two peaks of the u_z profile, which are solely the result of vortex-induced fluctuations, and represents a forced shear layer.

Since a large component of u' is the result of a random process which produces subharmonics of the basic instability frequency, phase scrambling takes place. The consequence of this can be seen in figure 19(a), which shows the profile of the autocorrelation coefficient $R_{uu}(\tau)$ at $x = 5.1\lambda_0$; note that near the shear layer centre,

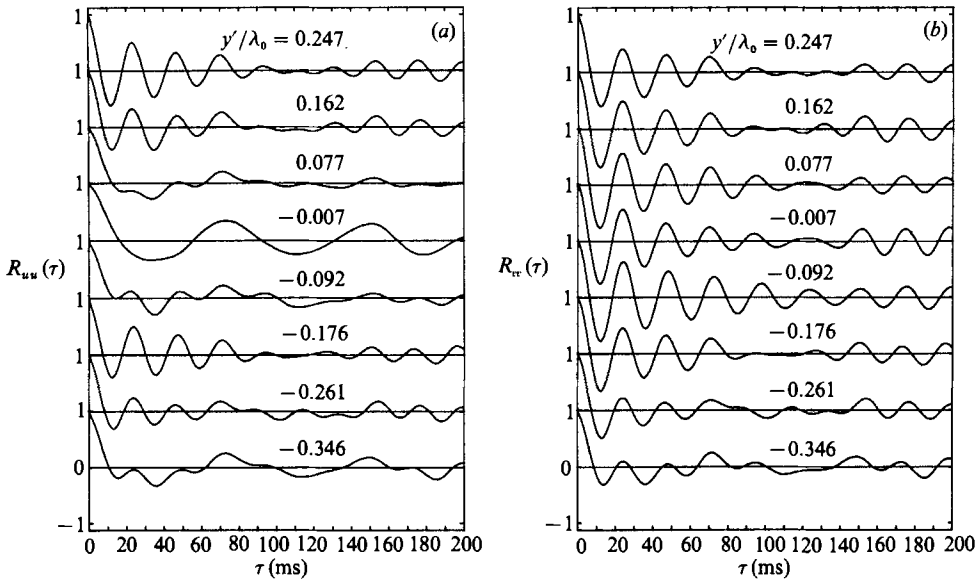


FIGURE 19. Profiles of the autocorrelation coefficients (a) $R_{uu}(\tau)$ and (b) $R_{vv}(\tau)$ at $x = 5.1\lambda_0$.

R_{uu} is unable to sift out the fundamental period but, instead, suggests an erroneously longer period. Other variations (such as, for example, in the strength of the vortices) have little or no effect on the magnitude of u' , since, over a long-time average, these tend to cancel out; they do, however, contribute to the broadening of the time-averaged profiles.

Figure 16 shows the transverse r.m.s. fluctuations v_z and v' , in which it should be noted that except for v' being broader than v_z , unlike their streamwise counterparts, they are very similar. That is, both exhibit a single peak with comparable magnitudes ($0.25\Delta U$ for v_z and $0.27\Delta U$ for v'). The reason for this is clear from figure 18(b), which shows that the transverse fluctuations induced by the passing vortices are generally similar, even when successive vortices pass on either side of the measurement point. For a forced shear layer the trace in figure 18(b) would look like a sine wave but still amount to about the same r.m.s. fluctuation. It is worth noting that $R_{vv}(\tau)$ (see figure 19b) is similar across a large part of the lateral extent of the shear layer.

Finally, figure 17 shows that no Reynolds stress is produced during the passage of a passive vortex or a row of aligned, equidistant such vortices (i.e. $-(uv)_z \approx 0$). On the other hand, $-\langle uv \rangle$ exhibits a single-peaked profile with a maximum value of about $0.009\Delta U^2$ (this is slightly less than half the largest peak value, measured at $x = 10.2\lambda_0$). This represents the fraction of vortices in the early stages of coalescence events (as discussed earlier in this section) during which the participant vortices are vertically displaced and drawn closer to each other. Thus, in agreement with the observations of previous investigators (Browand & Weidman 1976; Hussain & Zaman 1980) it is clear that passive vortices do not contribute at all to the production of large-scale Reynolds stress.

5. Summary and concluding remarks

A non-intrusive conditional-sampling technique, utilizing synchronized flow visualization and one-point, two-component laser-Doppler velocimetry, has been described. It was used to probe the dynamics of the vortex structure of a homogeneous plane shear layer, via conditional ensemble-averaged measurements. The novelty of using flow visualization as the conditioning agent offers the advantages of unambiguous detection and identification of the passing vortex, and instrumentation/processing simplicity.

Measurements were obtained for passive, first generation vortices at a station $6.2\lambda_0$ downstream of the splitter-plate trailing edge. Results included the ensemble-averaged velocity and vorticity fields of the average (of all ensembles) vortex. These indicate that, in this region, most of the vorticity is contained within the vortices, while no measurable circulation can be associated with the braid. Stagnation points exist on either side of the vortex featuring a straining field along the direction of the braid. The ensemble-averaged velocity field, in conjunction with the average vortex core (reconstructed from the statistical average of the vortex core features of all the ensembles), shows in some detail the process of entrainment of free-stream fluid by the vortices. Zone-average profiles, computed from the ensemble-averaged data, effectively remove jitter; as such, these can be interpreted as the time-averaged profiles of a forced shear layer. A comparison with actual time-averaged results, therefore, leads to an assessment of the effect of natural shear-layer jitter. This comparison suggests that, in general, jitter results in broader profiles; this is particularly so for second-order statistical quantities, such as u' and v' . Specifically though, variation in the lateral position of the passing vortices is responsible for large streamwise fluctuations, occurring between successive vortex passages, near the shear layer centreline. Owing to the random nature and the large contribution of these fluctuations, the r.m.s. fluctuation intensity u' and the autocorrelation coefficient R_{uu} are greatly affected. Through this comparison, it is also confirmed that a passive vortex does not contribute to the production of large-scale Reynolds stress, which is primarily the result of coalescence interactions.

As a final note on the conditional-sampling technique presented in this paper, it should be mentioned that there is room for improvement and refinement. The technique is, in principle, simple and its advantages are clear; reasonable and meaningful results are attainable as, we believe, has been demonstrated here. The difficulty, this being its major drawback, lies in the fact that it is considerably harder to process images rather than signals; also, automation is a task in itself, when working with images. Nonetheless, with the advent of faster and smarter image processing hardware and software, it is our belief that this technique can become an invaluable tool.

Support from the Office of Basic Energy Sciences of the Department of Energy under Contract DE-AC02-82ER 13003 is gratefully acknowledged. One of the authors (E.P.) also wishes to acknowledge the partial support of the Boris Bakhmeteff Research Fellowship in Fluid Mechanics.

REFERENCES

- BROWAND, F. K. & WEIDMAN, P. D. 1976 Large scales in the developing mixing layer. *J. Fluid Mech.* **76**, 127–144.
- BROWN, G. L. & ROSHKO, A. 1974 On density effects and large structure in turbulent mixing layers. *J. Fluid Mech.* **64**, 755–816.
- CHEVRAY, R. & TUTU, N. K. 1978 Intermittency and preferential transport of heat in a round jet. *J. Fluid Mech.* **88**, 133–160.
- COLES, D. 1981 Prospects for useful research on coherent structure in turbulent shear flow. *Proc. Indian Acad. Sci. (Engng Sci.)* **4**, 111–127.
- DAVIS, P. O. A. L. & YULE, A. J. 1975 Coherent structures in turbulence. *J. Fluid Mech.* **69**, 513–537.
- DIMOTAKIS, P. E. 1986 Two-dimensional shear layer entrainment. *AIAA J.* **24**, 1791–1796.
- DIMOTAKIS, P. E. & BROWN, G. L. 1976 The mixing layer at high Reynolds number: large structure dynamics and entrainment. *J. Fluid Mech.* **78**, 535–560.
- DIMOTAKIS, P. E., DEBUSSY, F. D. & KOCHESFAHANI, M. M. 1981 Particle streak velocity field measurements in a two dimensional mixing layer. *Phys. Fluids* **24**, 995–999.
- HERNAN, M. A. & JIMENEZ, L. 1982 Computer analysis of a high speed film of the plane turbulent mixing layer. *J. Fluid Mech.* **119**, 323–345.
- HO, C. M. & HUANG, S. 1982 Subharmonics and vortex merging in mixing layers. *J. Fluid Mech.* **119**, 443–473.
- HUSSAIN, A. K. M. F. 1983 Coherent structures – reality and myth. *Phys. Fluids* **26**, 2816–2850.
- HUSSAIN, A. K. M. F. & ZAMAN, K. B. M. Q. 1978 The free shear layer tone phenomenon and Kármán interference. *J. Fluid Mech.* **87**, 349–383.
- J. H. 1976 An experimental investigation of mixing in two dimensional turbulent shear flows with applications to diffusion limited chemical reactions. Ph.D. thesis, California Institute of Technology.
- KOCHESFAHANI, M. M., CATHERASOO, C. J., DIMOTAKIS, P. E., GHARIB, M. & LANG, D. B. 1979 Two-point LDV measurements in a plane mixing layer. *AIAA J.* **17**, 1347–1351.
- MOORE, D. W. & SAFFMAN, P. G. 1975 The density of organized vortices in a turbulent mixing layer. *J. Fluid Mech.* **69**, 465–473.
- MUMFORD, J. C. 1982 The structure of the large eddies in fully developed turbulent shear flows. Part 1. The plane jet. *J. Fluid Mech.* **118**, 214–268.
- PANIDES, E. 1987 On the vortical structure of a plane shear layer. Ph.D. thesis, Columbia University.
- ROBERTS, F. A. 1985 Effects of a periodic disturbance on structure and mixing in turbulent shear layers and wakes. Ph.D. thesis, California Institute of Technology.
- SOKOLOV, M., KLEIS, S. J. & HUSSAIN, A. K. M. F. 1981 Coherent structures induced by two simultaneous sparks in an axisymmetric jet. *AIAA J.* **19**, 1000–1008.
- STUART, J. T. 1967 On finite amplitude oscillations in laminar mixing layers. *J. Fluid Mech.* **29**, 417–440.
- WINANT, C. D. & BROWAND, F. K. 1974 Vortex pairing: the mechanism of turbulent mixing layer growth at a moderate Reynolds number. *J. Fluid Mech.* **63**, 237–255.
- YULE, A. J. 1978 Large scale structure in the mixing layer of a round jet. *J. Fluid Mech.* **89**, 413–432.
- ZAMAN, K. B. M. Q. & HUSSAIN, A. K. M. F. 1980 Vortex pairing in a circular jet under controlled excitation. *J. Fluid Mech.* **101**, 449–544.
- ZAMAN, K. B. M. Q. & HUSSAIN, A. K. M. F. 1981 Taylor hypothesis and large-scale coherent structures. *J. Fluid Mech.* **112**, 379–396.